galaxies

IMPACT FACTOR 3.8

CITESCORE 6.3

Article

Finite-Range Scalar–Tensor Gravity: Constraints from Cosmology and Galaxy Dynamics

Elie Almurr and Jean Claude Assaf

MDPI

https://doi.org/10.3390/galaxies14010007

galaxies

MDPI

Article

Finite-Range Scalar–Tensor Gravity: Constraints from Cosmology and Galaxy Dynamics

Elie Almurr * and Jean Claude Assaf

Faculty of Engineering, University of Balamand, Kalhat, Al-Kurah, Tripoli P.O. Box 100, Lebanon; jeanclaude.assaf@balamand.edu.lb

* Correspondence: elie.murr@std.balamand.edu.lb

Abstract

Objective: We examine whether a finite-range scalar–tensor modification of gravity can be simultaneously compatible with cosmological background data, galaxy rotation curves, and local/astrophysical consistency tests, while satisfying the luminal gravitational-wave propagation constraint ($c_T = 1$) implied by GW170817 at low redshifts. **Methods:** We formulate the model at the level of an explicit covariant action and derive the corresponding field equations; for cosmological inferences, we adopt an effective background closure in which the late-time dark-energy density is modulated by a smooth activation function characterized by a length scale λ and amplitude ϵ. We constrain this background model using Pantheon+, DESI Gaussian Baryon Acoustic Oscillations (BAOs), and a Planck acoustic-scale prior, including an explicit ΛCDM comparison. We then propagate the inferred characteristic length by fixing λ in the weak-field Yukawa kernel used to model 175 SPARC galaxy rotation curves with standard baryonic components and a controlled spherical approximation for the scalar response. **Results:** The joint background fit yields $\Omega_m = 0.293 \pm 0.007$, $\lambda = 7.69^{+1.85}_{-1.71}$ Mpc, and $H_0 = 72.33 \pm 0.50\,\mathrm{km\,s^{-1}\,Mpc^{-1}}$. With λ fixed, the baryons + scalar model describes the SPARC sample with a median reduced chi-square of $\chi^2_\nu = 1.07$; for a 14-galaxy subset, this model is moderately preferred over the standard baryons + NFW halo description in the finite-sample information criteria, with a mean ΔAICc outcome in favor of the baryons + scalar model ($\approx$2.8). A Vainshtein-type screening completion with $\Lambda = 1.3 \times 10^{-8}$ eV satisfies Cassini, Lunar Laser Ranging, and binary pulsar bounds while keeping the kpc scales effectively unscreened. For linear growth observables, we adopt a conservative General Relativity-like baseline ($\mu_0 = 0$) and show that current $f\sigma_8$ data are consistent with $\mu_0 \simeq 0$ for our best-fit background; the model predicts $S_8 = 0.791$, consistent with representative cosmic-shear constraints. **Conclusions:** Within the present scope (action-level weak-field dynamics for galaxy modeling plus an explicitly stated effective closure for background inference), the results support a mutually compatible characteristic length at the Mpc scale; however, a full perturbation-level implementation of the covariant theory remains an issue for future work, and the role of cold dark matter beyond galaxy scales is not ruled out.

Keywords: cosmology theory; dark energy; dark matter; galaxy kinematics and dynamics; gravitation; large-scale structure; statistical methods

Academic Editors: Jose L. Gómez and Lorenzo Iorio

Received: 20 November 2025
Revised: 31 December 2025
Accepted: 20 January 2026
Published: 27 January 2026

1. Introduction

The success of General Relativity (GR) across laboratory, solar system, and binary pulsar tests coexists with persistent large-scale phenomenology, including the late-time

acceleration of the cosmic expansion [1,2] and the apparent need for cold dark matter (CDM) in structural formation and galaxy dynamics [3,4]. ΛCDM considers this through a cosmological constant and a non-baryonic matter component [3]. An alternative program explores whether this phenomenology can partly arise from additional gravitational degrees of freedom, provided they are screened in high-density environments and are compatible with gravitational-wave (GW) constraints [5,6].

Scalar–tensor theories offer a well-controlled setting for these types of explorations. Among them, the subclass with derivative couplings to curvature (notably couplings to the Einstein tensor) is notable because it remains within the Horndeski/Lovelock framework of second-order field equations and can satisfy $c_T = 1$ [7,8]. For the scalar with a small mass, the associated fifth force has a finite range $\lambda = m^{-1}$, potentially allowing gravity to interpolate between GR-like behavior at short distances and modified behavior on astrophysical/cosmological scales.

This study explores a finite-range scalar–tensor theory within a single, consistent framework across two regimes: (i) cosmology, where we constrain a single length scale λ using background-expansion data, and (ii) galaxy dynamics, where we test whether the same λ can capture part of the observed rotation-curve phenomenology in the SPARC sample. To avoid ambiguity, we distinguish explicitly between results derived from the covariant action and those introduced as an effective phenomenological closure. Accordingly, we (a) express the full-field equations explicitly, (b) present the Friedmann–Lemaître–Robertson–Walker (FLRW) specialization, and (c) derive the weak-field limit and circular velocity expressions used in the SPARC analysis. Furthermore, we posit that the background expansion function used in the cosmological Markov Chain Monte Carlo (MCMC) is a phenomenological, coarse-grained closure motivated by void-percolation arguments and not a closed-form solution of the homogeneous scalar background.

The remainder of this paper is organized as follows. Section 2 introduces the action, defines parameters, and presents the field equations, conservation laws, GW speed, and FLRW specialization. Section 3 presents the effective background closure used for cosmological inference, data and likelihood, and the cosmological constraints (including an explicit ΛCDM comparison and cosmographic diagnostics). Section 4 derives the weak-field Yukawa limit, the modified potential, and the circular velocity used for SPARC fits and presents population-level results and morphology trends. Section 5 compares the scalar fits to standard Navarro–Frenk–White (NFW) halo fits for representative galaxies. Section 6 discusses additional consistency tests: screening across scales, growth-rate constraints, and peculiar-velocity bounds. Finally, Section 7 concludes the study. Supplementary tables are provided, and technical derivations are presented in appendices and explicitly cited in the main text.

2. Theoretical Framework and Field Equations

In this section, we establish the covariant formulation of the theory. We first present the action and define the coupling parameters, then derive the exact field equations and conservation laws. Finally, we establish the specific limits required for our analysis: the tensor propagation speed on cosmological backgrounds and the effective closure used for the expansion history.

2.1. Action and Parameter Definitions

We consider a scalar–tensor theory with a canonical scalar, a derivative coupling to the Einstein tensor, and a mass term that sets a finite interaction range [7,8]. The minimal action is

https://doi.org/10.3390/galaxies14010007

$$S_{\rm min} = \int d^4x\,\sqrt{-g}\left[\frac{M_{\rm Pl}^2}{2}R - \frac{1}{2}\,(\nabla\phi)^2 - \frac{\alpha}{2}\,G^{\mu\nu}\nabla_\mu\phi\nabla_\nu\phi - \frac{m^2}{2}\phi^2\right] + S_m\big[\tilde{g}_{\mu\nu},\psi_m\big], \quad (1)$$

where $M_{\rm Pl}$ is the reduced Planck mass, $G^{\mu\nu}$ is Einstein's tensor, and α is a coupling with dimensions of length^2. The scalar mass m defines a finite interaction range,

$$\lambda \equiv m^{-1}, \quad (2)$$

which is the central scale constrained in this work. We assume the matter fields ψ_m couple universally to a Jordan-frame metric $\tilde{g}_{\mu\nu}$. To ensure definiteness and to connect with the weak-field galaxy limit, we use a leading-order conformal coupling $\tilde{g}_{\mu\nu} = A^2(\phi)\,g_{\mu\nu}$ with $A(\phi) \simeq 1 + g\,\phi/M_{\rm Pl}$. This leading-order coupling generates an interaction of the form

$$S_{\rm int} \simeq -\frac{g}{M_{\rm Pl}}\int d^4x\,\sqrt{-g}\,\phi\,T, \quad (3)$$

where T is the trace of the matter energy–momentum tensor.

In high-density environments, derivative self-interactions can provide Vainshtein-type screening. To discuss screening across scales, we also consider an extended action with a cubic Galileon operator [9],

$$S = S_{\rm min} + \int d^4x\,\sqrt{-g}\Big[\frac{c_3}{\Lambda^3}(\nabla\phi)^2\Box\phi\Big], \quad (4)$$

with a dimensionless c_3 and a strong-coupling scale Λ. In the galaxy fits of Sections 4 and 5, we operate in a Yukawa regime where the cubic term is subdominant, but we use it in Section 6 to assess screening.

2.2. Metric and Scalar Field Equations

Varying the action with respect to the metric yields the modified Einstein equations,

$$M_{\rm Pl}^2\,G_{\mu\nu} = T^{(m)}_{\mu\nu} + T^{(\phi)}_{\mu\nu} + \alpha\,\Theta_{\mu\nu} + T^{(3)}_{\mu\nu}, \quad (5)$$

where $T^{(m)}_{\mu\nu}$ is the matter stress tensor (defined with respect to $g_{\mu\nu}$),

$$T^{(\phi)}_{\mu\nu} = \nabla_\mu\phi\nabla_\nu\phi - \frac{1}{2}g_{\mu\nu}(\nabla\phi)^2 - \frac{1}{2}m^2\phi^2 g_{\mu\nu}, \quad (6)$$

$\Theta_{\mu\nu}$ is the contribution from the Einstein's tensor coupling term, and $T^{(3)}_{\mu\nu}$ is the contribution from the cubic Galileon operator. As $\Theta_{\mu\nu}$ is lengthy, we introduce its explicit covariant form in Appendix A and use Equation (5) in the main text as the definition of our field equations.

Varying the action with respect to ϕ yields

$$\Box\phi - m^2\phi + \alpha\,G^{\mu\nu}\nabla_\mu\nabla_\nu\phi + \frac{c_3}{\Lambda^3}\Big[(\Box\phi)^2 - \nabla_\mu\nabla_\nu\phi\,\nabla^\mu\nabla^\nu\phi - R_{\mu\nu}\nabla^\mu\phi\nabla^\nu\phi\Big] = \frac{g}{M_{\rm Pl}}\,T. \quad (7)$$

In the weak-field and quasi-static regimes relevant to galaxies, the curvature-dependent terms are subleading, and Equation (7) reduces to a Yukawa-type equation, as shown in Section 4.

2.3. Conservation Laws and Frames

The Bianchi identity $\nabla_\mu G^{\mu\nu} = 0$ implies covariant conservation of the total stress tensor on the right-hand side of Equation (5). If matter is minimally coupled in the Jordan

frame $\tilde{g}_{\mu\nu}$, then $\tilde{\nabla}_\mu \tilde{T}^{\mu\nu}_{(m)} = 0$ holds with respect to $\tilde{g}_{\mu\nu}$. In the Einstein frame $g_{\mu\nu}$, and for $A(\phi) \neq 1$, the matter stress tensor is not separately conserved; at the leading order,

$$\nabla_\mu T^{\mu\nu}_{(m)} \simeq \frac{g}{M_{\rm Pl}}\, T\, \nabla^\nu \phi, \tag{8}$$

which corresponds to an exchange of energy–momentum between matter and the scalar. In this study, the baryonic mass models used in galaxy fits are treated as stationary sources in the quasi-static limit, and the scalar-mediated force is encoded in the modified potential derived from Equation (7).

2.4. Gravitational-Wave Speed

In Horndeski-class scalar–tensor theories, the observation of GW170817/GRB170817A [10] constrains the low-redshift tensor speed to be extremely close to the speed of light. For the derivative coupling to the Einstein tensor in Equation (1), tensor perturbations around an FLRW background propagate with

$$c_T^2 = 1, \tag{9}$$

so that the theory is compatible with the GW170817 constraint at low redshifts (refer to the references [11,12]). We emphasize that GW170817 is a low-z event, and future, higher redshift multimessenger observations can test possible temporal dependencies of GW propagation in broader effective-field-theory frameworks [13,14].

2.5. FLRW Specialization Derived from the Action

For a spatially flat FLRW metric with a scale factor $a(t)$ and a homogeneous scalar $\phi(t)$, Equations (5)–(7) reduce to generalized Friedmann equations. Based on the expression

$$3M_{\rm Pl}^2 H^2 = \rho_m + \rho_r + \rho_\phi, \qquad -2M_{\rm Pl}^2 \dot{H} = (\rho_m + p_m) + (\rho_r + p_r) + (\rho_\phi + p_\phi), \tag{10}$$

the effective scalar energy density and pressure for the Einstein tensor coupling (with $c_3 = 0$) take the standard form [8]

$$\rho_\phi = \frac{1}{2}\dot{\phi}^2\left(1 + 9\alpha H^2\right) + \frac{1}{2}m^2\phi^2, \tag{11}$$

$$p_\phi = \frac{1}{2}\dot{\phi}^2\left(1 - 3\alpha H^2 - 2\alpha\dot{H}\right) - \frac{1}{2}m^2\phi^2 - 2\alpha H\dot{\phi}\,\ddot{\phi}, \tag{12}$$

and the homogeneous scalar equation becomes

$$\left(1 + 3\alpha H^2\right)\ddot{\phi} + 3H\left(1 + 3\alpha H^2 + 2\alpha\dot{H}\right)\dot{\phi} + m^2\phi = \frac{g}{M_{\rm Pl}}\, T. \tag{13}$$

These equations provide the action-level cosmological dynamics of the model.

2.6. Effective Background Closure Used for Cosmological Inference

In this study, we do not claim to integrate the coupled FLRW system presented above for $\phi(t)$ and $a(t)$. Instead, following a coarse-graining/void-percolation motivation, we close the background expansion phenomenologically by introducing an effective activation function $F(a)$ that modulates the dark-energy density at later times. This key phenomenological component in our cosmological inference is introduced explicitly as an effective closure.

We parameterize the activation as

$$F(a) \equiv \frac{f(a)}{f(1)}, \qquad f(a) = \epsilon\,\frac{1}{2}\left[1 + \tanh\left(2\left(\frac{R_0\, a}{\lambda} - 1\right)\right)\right], \tag{14}$$

where R_0 is a characteristic co-moving scale associated with the present-day void network (we adopt $R_0 = 35$ Mpc as a representative value), and ϵ is an effective normalization parameter. The ratio $f(a)/f(1)$ ensures that $F(1) = 1$ so that $\Omega_{\rm DE}$ remains the present-day dark-energy fraction. Importantly, Equation (14) is not derived as a closed-form homogeneous solution of the scalar background in Section 2; it is an effective closure used only for the background expansion. This choice of scope is explicitly discussed again in Sections 3 and 7.

With this closure, the effective Hubble function used in the cosmological likelihood is

$$H^2(z) = H_0^2\left[\Omega_m(1+z)^3 + \Omega_r(1+z)^4 + \Omega_{\rm DE}\,F\left(\frac{1}{1+z}\right)\right], \tag{15}$$

where $\Omega_{\rm DE} = 1 - \Omega_m - \Omega_r$ and Ω_r is fixed by $T_{\rm CMB}$ and $N_{\rm eff}$. Equation (15) is the background model used in our MCMC; it must be considered an effective description rather than the exact solution of the homogeneous scalar dynamics.

3. Cosmological Constraints from Background Data

3.1. Data and Likelihood

We constrain the effective background model (15) using (i) the Pantheon+ supernova compilation [15,16] (with analytic marginalization over the SN absolute magnitude), (ii) BAO distance measurements, including DESI Gaussian BAO constraints [17] (used in the standard D_M/r_d, D_H/r_d, and D_V/r_d combinations), and (iii) the Planck acoustic-scale prior ℓ_A [3]. The total likelihood is the product of the individual likelihoods; for independent datasets, we add their χ^2 contributions,

$$\chi^2_{\rm tot} = \chi^2_{\rm SN} + \chi^2_{\rm BAO} + \chi^2_{\ell_A}. \tag{16}$$

For supernovae, we use the standard, analytically marginalized form (see Appendix C for details and notation),

$$\chi^2_{\rm SN} = A - \frac{B^2}{C}, \tag{17}$$

with A, B, and C defined from the Pantheon+ covariance matrix. For BAO, we use

$$D_M(z) = c\int_0^z \frac{dz'}{H(z')}, \tag{18}$$

$$D_H(z) = \frac{c}{H(z)}, \tag{19}$$

$$D_V(z) = \left[z\,D_M^2(z)\,D_H(z)\right]^{1/3}, \tag{20}$$

and compare the outcomes to the published r_d scaled measurements. For the acoustic scale, we adopted a Gaussian prior on ℓ_A with mean and variance values obtained from Planck [3].

3.2. Sampling and Priors

We explore the posterior of $(\Omega_m, \lambda, \epsilon, H_0)$ with an affine-invariant ensemble sampler. Priors and convergence diagnostics are summarized in Appendix C and Table S3 (Supplementary Materials).

3.3. Cosmological Posteriors and Best-Fit Values

The posterior constraints are shown in Figure 1. We obtained (posterior medians and 68% credible intervals)

$$\Omega_m = 0.293^{+0.007}_{-0.007}, \qquad \lambda = 7.69^{+1.85}_{-1.71}\,\mathrm{Mpc}, \qquad H_0 = 72.33^{+0.50}_{-0.49}\,\mathrm{km\,s^{-1}\,Mpc^{-1}}, \tag{21}$$

with ϵ weakly constrained because of the normalization $F(1) = 1$ in Equation (14). We emphasize that the cosmological inference constrains the activation scale λ that enters the effective closure, which is propagated to the galaxy sector as a fixed interaction range.

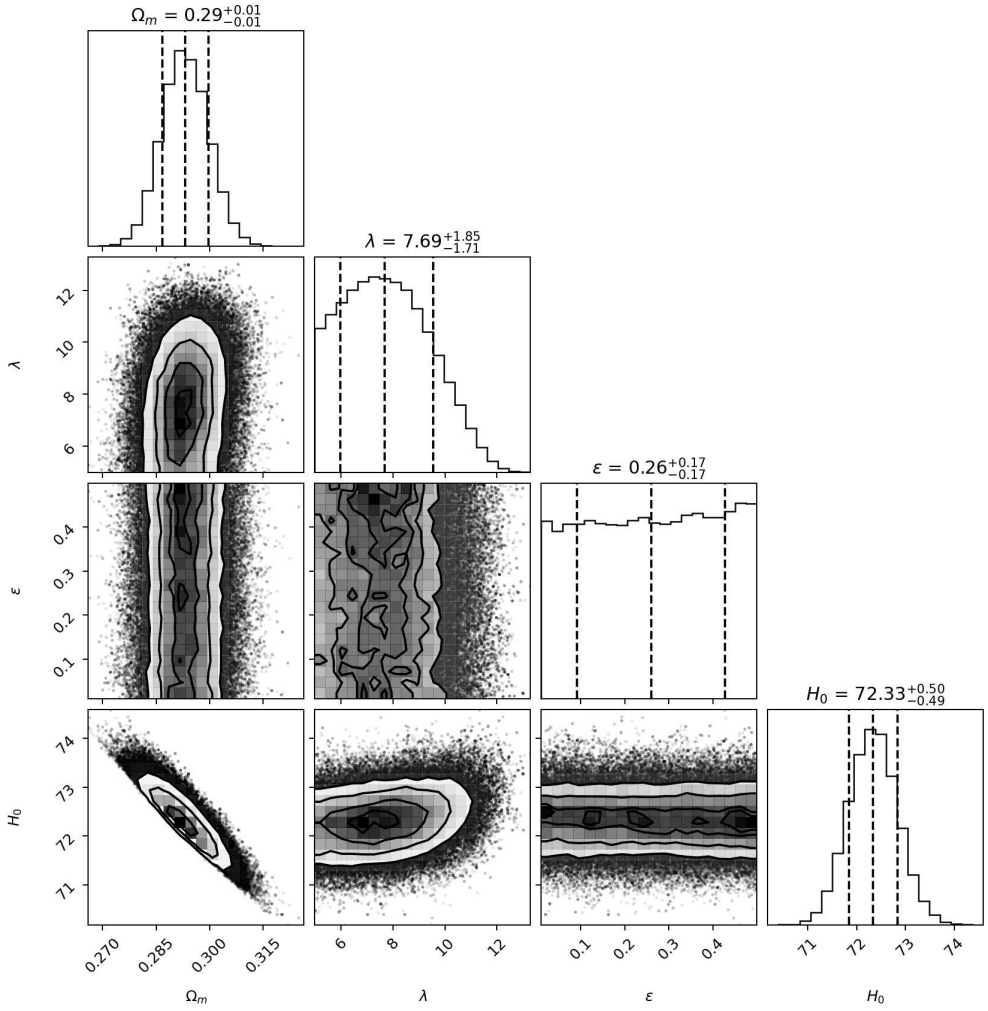

Figure 1. Cosmological posterior for the effective background model (15) using Pantheon+, BAO, and the acoustic-scale prior. The inner and outer contours represent 68% and 95% confidence intervals, respectively, and the dashed lines in the histograms indicate the 16th, 50th, and 84th percentiles.

3.4. ΛCDM Comparison and Cosmographic Diagnostics

To address model comparison explicitly, we fitted the same datasets with a ΛCDM baseline (constant dark-energy density, i.e., $F(a) = 1$) and compared the minimum χ^2 and Akaike information criterion (AIC) outcomes. Table 1 summarizes the results. The improvement in χ^2 relative to ΛCDM is negligible, and the extra parameters of the effective activation model are therefore disfavored by AIC, as expected for a minimal background data comparison.

We also report basic cosmographic diagnostics derived from the best-fitted $H(z)$; the present-day deceleration parameter $q_0 \simeq -0.56$ and jerk $j_0 \simeq 1.00$, and the $Om(z)$ diagnostic remains almost constant within the range of $z \lesssim 2.5$ (see Appendix D).

Table 1. Comparison to a ΛCDM baseline using the same background datasets.

Model	Parameters	$\chi^2_{\min}$	ΔAIC
ΛCDM	(Ω_m, H_0)	15,455.45	0
Effective activation ($F(a)$)	$(\Omega_m, \lambda, \epsilon, H_0)$	15,455.54	4.09

4. Galaxy Dynamics and SPARC Rotation Curves

4.1. Weak-Field Limit and Modified Potential

In the weak-field regime around Minkowski's space, curvature terms are negligible ($G_{\mu\nu} \approx 0$) and the scalar Equation (7) reduces to a Yukawa equation,

$$\left(\nabla^2 - m^2\right)\phi \simeq \frac{g}{M_{\rm Pl}}\,\rho_b, \tag{22}$$

where ρ_b is the (nonrelativistic) baryonic density. The solution to Green's function is

$$\phi(\mathbf{r}) = -\frac{g}{4\pi M_{\rm Pl}} \int d^3\mathbf{r}'\, \frac{\rho_b(\mathbf{r}')\, e^{-|\mathbf{r}-\mathbf{r}'|/\lambda}}{|\mathbf{r}-\mathbf{r}'|}. \tag{23}$$

For conformal matter coupling $A(\phi) \simeq 1 + g\phi/M_{\rm Pl}$, the scalar-mediated acceleration of a test particle is $\mathbf{a}_\phi \simeq -(g/M_{\rm Pl})\nabla\phi$. Defining an effective scalar potential $\Phi_\phi \equiv g\phi/M_{\rm Pl}$, we have $\mathbf{a}_\phi = -\nabla\Phi_\phi$. In spherical symmetry, Equation (22) can be reduced to one-dimensional integrals; the explicit kernel and the form used in the numerical fits are derived in Appendix B.

The total potential is

$$\Phi(r) = \Phi_N(r) + \Phi_\phi(r), \tag{24}$$

where Φ_N is the Newtonian potential sourced by baryons. The circular velocity of particles in stable circular orbits is then

$$v_c^2(r) = r\,\frac{d\Phi}{dr} = v_b^2(r) + v_\phi^2(r), \tag{25}$$

with $v_b(r)$ being the standard baryonic contribution and $v_\phi^2(r) \equiv r\,|a_\phi(r)|$.

4.2. Practical Implementation for SPARC Fits

We use the SPARC database of rotation curves and baryonic components herein. For each galaxy, SPARC provides the gas, disk, and bulge contributions to the rotation curve under a fiducial mass-to-light ratio. We express the baryonic contribution as

$$v_b^2(r) = v_{\rm gas}^2(r) + \Upsilon_\star\left[v_{\rm disk}^2(r) + v_{\rm bulge}^2(r)\right], \tag{26}$$

where $\Upsilon_\star$ is a free stellar mass-to-light parameter. Given $v_b(r)$, we reconstruct an effective spherical baryonic density profile via

$$\rho_b(r) = \frac{1}{4\pi r^2}\,\frac{d}{dr}\left(\frac{r\,v_b^2(r)}{G}\right), \tag{27}$$

which is exact for spherical mass distributions and provides an effective radial source for the Yukawa kernel.

4.3. Spherical Symmetry Assumption and Robustness

The SPARC baryonic components are disk-like rather than spherical. Our scalar-force kernel, however, is evaluated by assuming spherical symmetry for tractable analysis across the full sample and because the scalar field depends primarily on the enclosed mass profile in the quasi-static regime. We therefore adopted spherical symmetry as a controlled approximation for the population study. Appendix E summarizes its scope and limitations for disk-like baryonic components, and an explicitly axisymmetric implementation is deferred to future work.

4.4. Galaxy-Level Inference and Fixed-λ Analysis

Herein, we adopt the cosmological posterior median $\lambda = 7.69$ Mpc (i.e., $\lambda = 7.69 \times 10^3$ kpc) and maintain it for all SPARC galaxies, interpreting it as the Yukawa range parameter appearing in the weak-field solution of Equation (22) (see Appendix B for the explicit spherical kernel used in the pipeline). For each galaxy, we sample the posterior over the parameter set $(g, \Upsilon_\star, \sigma_{\rm sys}, \sigma_{\rm turb})$, where $\sigma_{\rm sys}$ and $\sigma_{\rm turb}$ are non-negative nuisance dispersions added in quadrature to the reported SPARC velocity uncertainties, $\sigma_i^2 = \sigma_{i,\rm SPARC}^2 + \sigma_{\rm sys}^2 + \sigma_{\rm turb}^2$, to account for residual systematics and noncircular motions. We report the posterior median model and a 68% credible band; unless stated otherwise, quoted constraints refer to g and $\Upsilon_\star$ with $(\sigma_{\rm sys}, \sigma_{\rm turb})$ marginalized.

Figures 2 and 3 show representative fits for NGC7814 (high surface brightness) and PGC51017 (low surface brightness), illustrating the range of rotation-curve morphologies captured by the baryons + scalar model with a fixed λ value.

4.5. Population Results, Goodness of Fit, and Morphology

We found a median reduced chi-square value of $\chi^2_\nu \simeq 1.07$ (Supplementary Table S2) across the full sample with a tail at higher χ^2_ν values. Figure 4 shows the distribution. We report representative galaxies in Table 2 and provide full-sample fit summaries in Table S1.

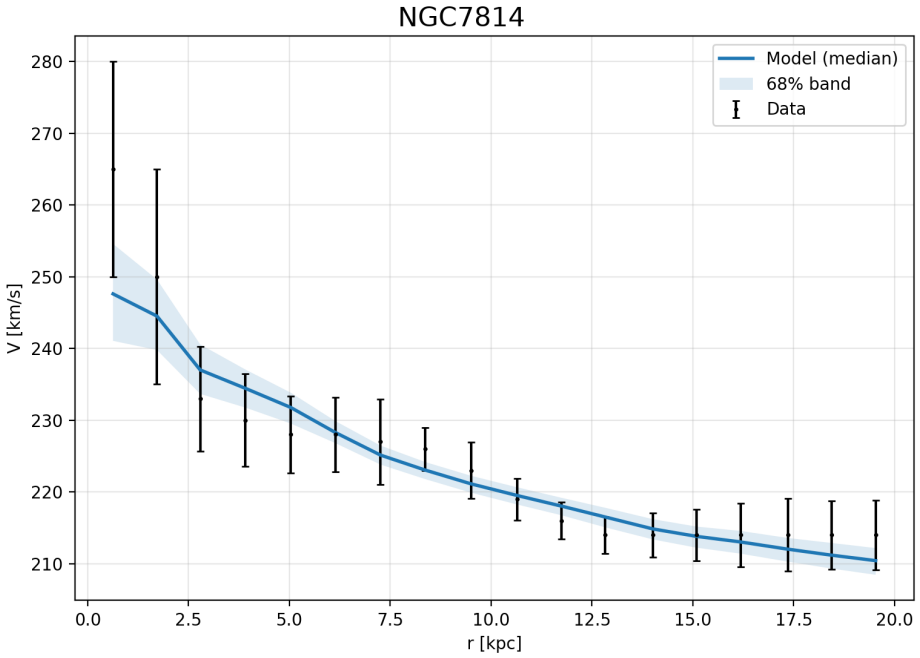

Figure 2. Representative SPARC fit for NGC7814 using baryons + scalar with λ fixed to the cosmological posterior median. The solid curve is the posterior median model, and the shaded region is the 68% credible band.

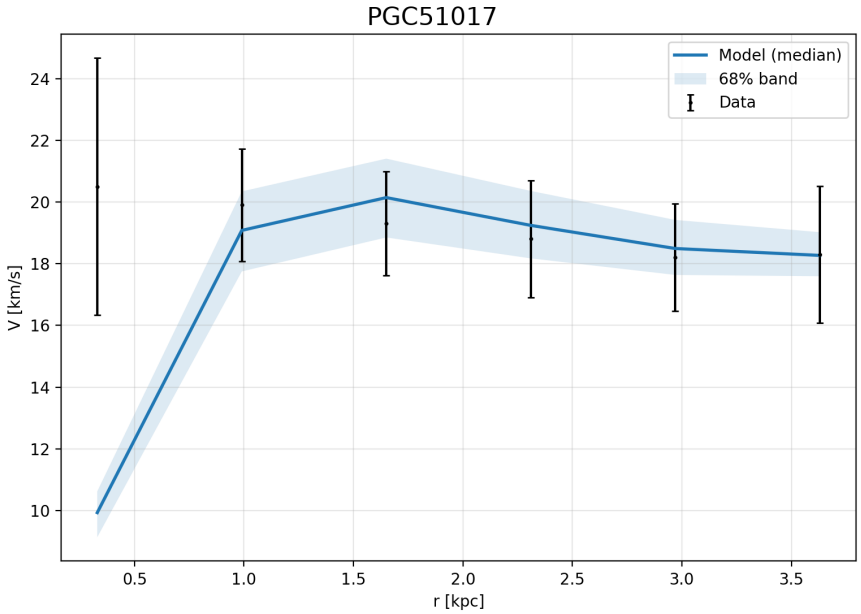

Figure 3. Representative SPARC fit for PGC51017 using baryons + scalar with λ fixed to the cosmological posterior median.

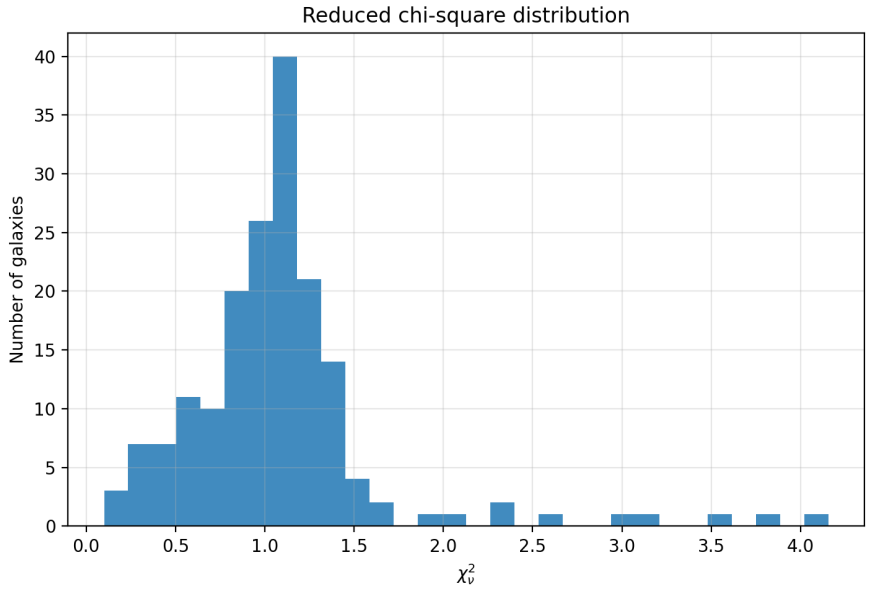

Figure 4. Distribution of reduced chi-square values for baryons + scalar fits across the SPARC sample (fixed λ).

Table 2. Representative SPARC galaxies spanning different fit qualities and morphologies (see Table S1 for the full sample). Values are posterior medians, and χ^2_ν is the reduced chi-square.

Galaxy	Morphology	g	$\Upsilon_\star$	χ^2_ν
UGC05005	Irr/LSB	0.0403	0.567	0.072
F574-2	Sa–Sb	0.00062	0.547	0.277

We also examined the trends in morphology using a coarse two-bin classification scheme (early-type spirals Sa–Sb versus irregular/LSB systems). Figure 5 shows that the inferred coupling g exhibits a mild morphology dependence in this binning, with Sa–Sb systems

tending to slightly higher median g values than Irr/LSB galaxies. We emphasize that this is an empirical trend within the model and does not imply a unique causal interpretation.

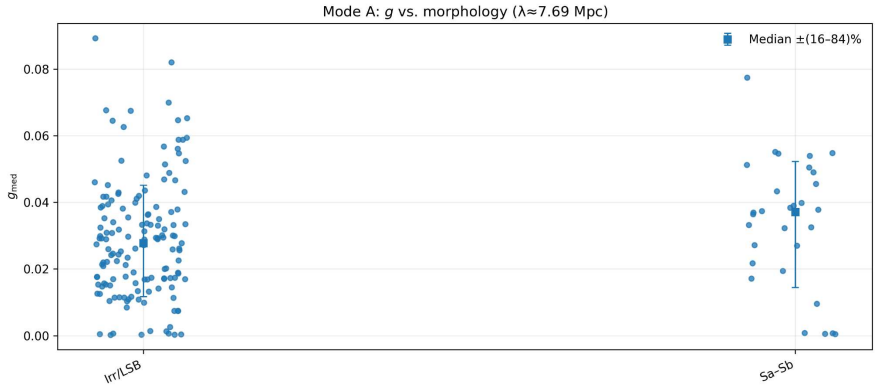

Figure 5. Mode A: Inferred scalar coupling g versus morphology for the SPARC sample, with λ fixed to the cosmological posterior median. Points show individual galaxies; squares show the median and 16–84% interval in each morphology bin.

5. Halo-Model Comparison

A key question is whether the baryons + scalar fits effectively replace a standard dark-matter halo or whether a halo component is still preferred in some systems. To illustrate this, we performed fits to representative galaxies under three models with a fixed λ value: (i) baryons + scalar, (ii) baryons + NFW, and (iii) a combined model (baryons + scalar + NFW). Figure 6 shows the comparison for three illustrative galaxies. In some cases, the baryons + scalar and baryons + NFW models achieve comparable χ^2_ν, while the combined model can reduce the residual structure at the cost of additional parameters.

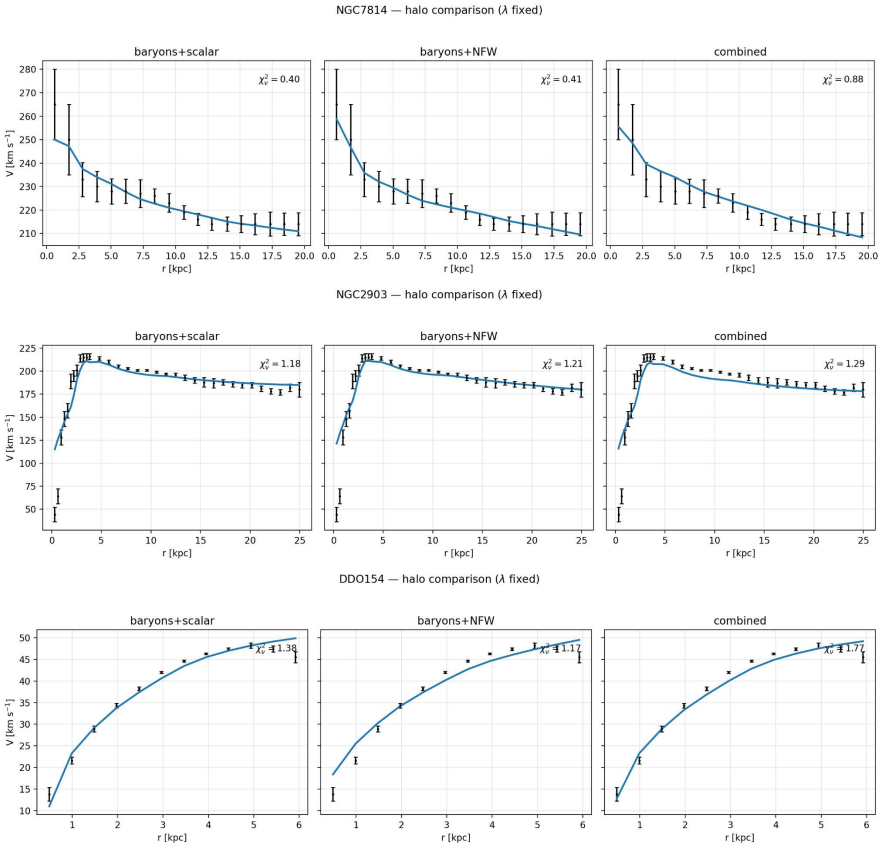

Figure 6. Comparison of baryons + scalar, baryons + NFW, and combined fits for representative galaxies with λ fixed.

6. Additional Consistency Tests and Constraints

6.1. Screening Across Scales

To connect the finite-range interaction to local tests, we examined screening using the cubic Galileon operator in Equation (4). Figure 7 summarizes the screening factor across the solar system, galaxy, and cluster scales for parameter choices consistent with our inferred λ. The solar system panel includes the Cassini scale based on [18].

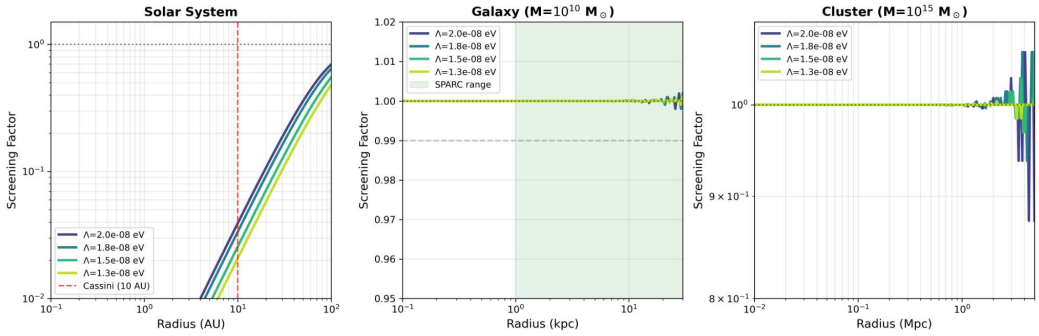

Figure 7. Screening factor across the solar system, galaxy, and cluster scales for representative parameter choices. The light green shaded region in the central panel indicates the radial range probed by SPARC rotation curves (1–30 kpc), and the grey dashed line marks the threshold where the scalar force is 99% unscreened. Notation such as 1.5E-8 in the figure corresponds to 1.5×10^{-8}.

6.2. Growth of Structure and σ_8

Our cosmological inference uses background observables. In scalar–tensor theories, perturbations can induce time- and scale-dependent modifications to the effective gravitational coupling $\mu(z, k)$ and the gravitational slip. We adopted a conservative baseline with $\mu_0 = 0$ in the growth analysis. Evolving dark-energy perturbations can modify μ and hence affect $f\sigma_8$ and σ_8, as emphasized recently by [19]. We therefore treat μ_0 as a possible nuisance degree of freedom and show in Appendix F that current $f\sigma_8$ data are consistent with $\mu_0 \simeq 0$ (within the uncertainty range) for our background best fit. A full Boltzmann-code implementation of the covariant action (1) at the perturbation level is beyond the scope of this study and constitutes future work.

6.3. Peculiar-Velocity Floor

A finite-range modification can also affect large-scale peculiar velocities. We compile peculiar velocity measurements and compare them to an envelope implied by the best-fit activation scale. Figure 8 shows the resulting constraint, which places a conservative upper bound on the impact of the finite-range interaction on low-redshift velocities.

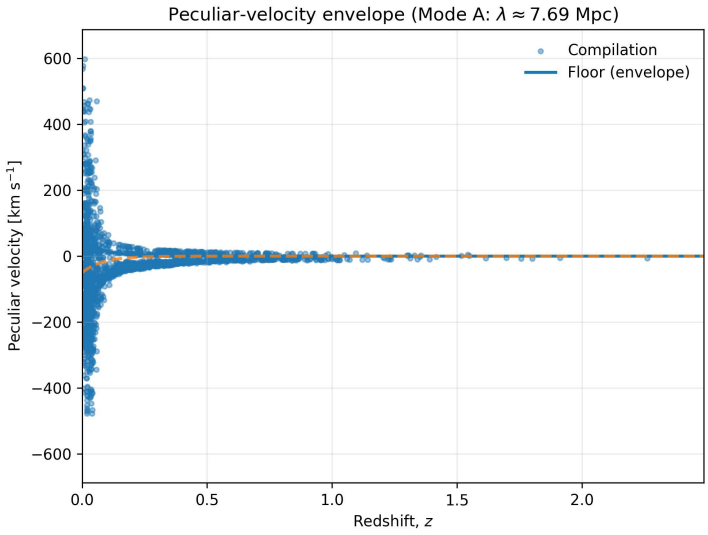

Figure 8. Peculiar- velocity envelope for Mode A with λ fixed to the cosmological posterior median.

7. Conclusions

We enforce conceptual consistency between the covariant scalar–tensor theory and the phenomenological components used in cosmology and galaxy dynamics by explicitly separating action-derived results from effective closures. Our main results are the following:

- We formulated the theory at the explicit action level and provided the full-field equations from metric and scalar variations (Section 2, Appendix A). The theory satisfies $c_T = 1$ and is compatible with GW170817 at low redshifts, while higher z multimessenger tests remain important (Section 2).
- We derived the FLRW specialization from the action and formulated the generalized Friedmann and scalar background equations. We then made a deliberate scope choice: the background expansion used for cosmological inference was considered an effective closure (Equation (14)), motivated by coarse-graining/void-percolation arguments and not claimed to be a closed-form solution of the homogeneous scalar dynamics.
- Using Pantheon+, BAO, and the acoustic scale, we constrained the activation length to $\lambda \simeq 7.7$ Mpc and obtained a background expansion close to ΛCDM in cosmographic diagnostics. We also included an explicit ΛCDM comparison via information criteria (Section 3).
- Fixing λ to the cosmological posterior median, we derived the weak-field Yukawa limit and used it to fit SPARC rotation curves. We obtained statistically acceptable fits for a large fraction of the sample (median $\chi^2_\nu \simeq 1.07$) and documented population statistics, morphology trends, and representative examples (Section 4).
- We compared scalar fits to standard NFW halo fits for representative galaxies and discussed screening, growth, and peculiar-velocity constraints (Sections 5 and 6).

The logical structure is explicit, indicating that the covariant action defines the modified gravity theory and its local/weak-field behavior, while the late-time background expansion used in the cosmological likelihood is an effective phenomenological closure. Once this separation is made explicit, the paper provides a coherent and testable set of constraints on a finite interaction range across cosmology and galaxy dynamics.

Supplementary Materials: The following supporting information can be downloaded at https://www.mdpi.com/article/10.3390/galaxies14010007/s1, Table S1: full SPARC fit summary; Table S2: population statistics and morphology bins; Table S3: cosmology convergence diagnostics; Table S4: sensitivity tests; and Table S5: galaxy fits for alternative fixed λ values.

Author Contributions: Conceptualization: E.A. and J.C.A.; methodology: E.A.; software: E.A.; validation: E.A.; formal analysis: E.A.; investigation: E.A.; resources: E.A. and J.C.A.; data curation: E.A.; writing—original draft preparation: E.A.; writing—review and editing: E.A. and J.C.A.; visualization: E.A.; supervision: J.C.A. All authors have read and agreed to the published version of the manuscript.

Funding: This research received no external funding.

Institutional Review Board Statement: Not applicable.

Informed Consent Statement: Not applicable.

Data Availability Statement: All data products used in this study are either public (Pantheon+, BAO compilations, Planck acoustic scale, and SPARC) or provided as supplementary tables in the manuscript. The analysis scripts used to generate the results are available from the corresponding author upon reasonable request.

Acknowledgments: We thank the anonymous reviewers for their constructive criticism that substantially improved the conceptual clarity and presentation of the manuscript.

Conflicts of Interest: The authors declare no conflicts of interest.

Appendix A. Einstein's Tensor Coupling Contribution $\Theta_{\mu\nu}$

For completeness, we record the covariant expression for the metric variation of the Einstein's tensor coupling term in Equation (1). According to standard results in the literature [8], the contribution $\Theta_{\mu\nu}$ listed in Equation (5) is

$$\begin{aligned}\Theta_{\mu\nu} = & -\frac{1}{2}\nabla_\mu\phi\nabla_\nu\phi\, R + 2\,\nabla_\alpha\phi\,\nabla_{(\mu}\phi\, R_{\nu)}{}^{\alpha} + \nabla^\alpha\phi\nabla^\beta\phi\, R_{\mu\alpha\nu\beta} + \nabla_\mu\nabla^\alpha\phi\,\nabla_\nu\nabla_\alpha\phi - \nabla_\mu\nabla_\nu\phi\,\Box\phi \\ & -\frac{1}{2}\,G_{\mu\nu}(\nabla\phi)^2 + g_{\mu\nu}\left[-\frac{1}{2}\,\nabla^\alpha\nabla^\beta\phi\,\nabla_\alpha\nabla_\beta\phi + \frac{1}{2}\,(\Box\phi)^2 - \nabla_\alpha\phi\nabla_\beta\phi\, R^{\alpha\beta}\right]. \end{aligned} \tag{A1}$$

Appendix B. Spherically Symmetric Yukawa Kernel and Acceleration

We derive herein the spherically symmetric form of the Yukawa potential and the acceleration used in the SPARC fits. Starting from Equation (22) and assuming $\rho_b = \rho_b(r)$, the solution can be written in terms of one-dimensional integrals. Differentiating the resulting potential yields an acceleration of the form

$$a_\phi(r) = -\frac{g^2}{4\pi}\left[A(r) - e^{-r/\lambda}B(r)\right], \tag{A2}$$

with

$$A(r) = \frac{1}{r^2}\int_0^r dr'\, r'^2\,\rho_b(r'), \qquad B(r) = \frac{1}{r}\int_0^r dr'\, r'\,\rho_b(r')\,\frac{\sinh(r'/\lambda)}{r'/\lambda}. \tag{A3}$$

These are the expressions implemented in the analysis scripts.

Appendix C. Cosmological Likelihood Details

This appendix summarizes the likelihood components and sampling choices used in Section 3.

Appendix C.1. Supernovae

For each SN at redshift z_i, we compute the theoretical distance modulus $\mu_{\rm th}(z_i) = 5\log_{10}[D_L(z_i)/{\rm Mpc}] + 25$, where $D_L(z) = (1+z)D_M(z)$ and $D_M(z)$ is given by Equation (18). Defining $\Delta\boldsymbol{\mu} = \boldsymbol{\mu}_{\rm obs} - \boldsymbol{\mu}_{\rm th}$ and using the Pantheon+ covariance matrix $\mathbf{C}_{\rm SN}$, we construct $A = \Delta\boldsymbol{\mu}^T\mathbf{C}_{\rm SN}^{-1}\Delta\boldsymbol{\mu}$, $B = \mathbf{1}^T\mathbf{C}_{\rm SN}^{-1}\Delta\boldsymbol{\mu}$, $C = \mathbf{1}^T\mathbf{C}_{\rm SN}^{-1}\mathbf{1}$. Analytically marginalizing over the SN absolute magnitude yields Equation (17): $\chi^2_{\rm SN} = A - B^2/C$.

Appendix C.2. BAO

For each BAO measurement, we compute the values of $D_M(z)$, $D_H(z)$, and $D_V(z)$ (Equations (18)–(20)) and compare them with the published scaled r_d values using the corresponding covariance matrices.

Appendix C.3. Acoustic Scale

We herein adopt a Gaussian prior on the acoustic scale ℓ_A with a mean of $\ell_A = 301.471$ and a standard deviation of $\sigma_{\ell_A} = 0.090$, consistent with Planck [3] (as implemented in the analysis code).

Appendix C.4. Priors and Sampling

We sample the posterior in $(\Omega_m, \lambda, \epsilon, H_0)$ with flat priors as follows: $\Omega_m \in [0.10, 0.50]$, $\lambda \in [5, 50]$ Mpc, and $\epsilon \in [0.01, 0.50]$, $H_0 \in [60, 80]$ km s^{-1} Mpc^{-1}. We also use an affine-invariant ensemble sampler with 32 walkers and 8000 steps, discarding the first 2000 as burn-in. Convergence was assessed using the integrated autocorrelation time, and findings are summarized in Supplementary Table S3.

Appendix D. Cosmographic Diagnostics

We herein define the deceleration parameters $q(z)$, jerk $j(z)$, and $Om(z)$ diagnostic as

$$q(z) = -1 + \frac{1+z}{H(z)}\frac{dH}{dz}, \qquad Om(z) = \frac{E^2(z) - 1}{(1+z)^3 - 1}, \tag{A4}$$

with $E(z) \equiv H(z)/H_0$. For the best-fit parameters in Section 3, we found that $q_0 \simeq -0.56$ and $j_0 \simeq 1.00$, which are in close agreement with the ΛCDM values.

Appendix E. Spherical Symmetry Approximation

We model disk galaxies using a spherical reconstruction of the baryonic source in the Yukawa kernel, derived from the observed radial baryonic contribution $v_b(r)$ (Section 4.3). This choice enables a uniform, tractable pipeline across the full SPARC sample but introduces a geometric systematic for flattened mass distributions. A dedicated axisymmetric implementation (e.g., evaluating the Yukawa potential of disk components in the mid-plane), together with a quantitative validation of its impact on inferred parameters, is deferred to future work. Accordingly, spherical symmetry should be viewed as a controlled approximation in the present analysis rather than an exact treatment of disk geometry.

Appendix F. Growth-Rate Nuisance Parameter Test

We briefly summarize the nuisance test in which we allow a scale-independent modification of the effective gravitational coupling in the linear growth sector, parameterized by an effective amplitude μ_0, while maintaining the background fixed to the best-fit parameters. Using a compilation of $f\sigma_8$ measurements (20 points), the baseline case with $\mu_0 = 0$ yields $\chi^2 \simeq 17.07$ (reduced $\chi^2 \simeq 0.95$ for 18 degrees of freedom, fitting only an overall normalization σ_8). Allowing μ_0 as an additional free parameter yields the best-fit outcome of $\mu_0 \simeq -0.02$ with $\chi^2 \simeq 16.83$, i.e., $\Delta\chi^2 \simeq 0.24$ for one extra parameter; information criteria therefore do not favor the introduction of μ_0 (for example, ΔAIC $\simeq +1.76$). This supports treating $\mu_0 = 0$ as a conservative baseline given current data, while emphasizing that a full perturbation-level (Boltzmann-code) implementation of the covariant action constitutes future work.

References

1. Carroll, S.M. The Cosmological Constant. *Living Rev. Relativ.* **2001**, *4*, 1. [CrossRef] [PubMed]
2. Weinberg, S. The Cosmological Constant Problem. *Rev. Mod. Phys.* **1989**, *61*, 1–23. [CrossRef]
3. Planck Collaboration. Planck 2018 Results. VI. Cosmological Parameters. *Astron. Astrophys.* **2020**, *641*, A6. [CrossRef]
4. Peebles, P.J.E. *Principles of Physical Cosmology*; Princeton University Press: Princeton, NJ, USA, 1993.
5. Clifton, T.; Ferreira, P.G.; Padilla, A.; Skordis, C. Modified Gravity and Cosmology. *Phys. Rep.* **2012**, *513*, 1–189. [CrossRef]
6. Joyce, A.; Jain, B.; Khoury, J.; Trodden, M. Beyond the Cosmological Standard Model. *Phys. Rep.* **2015**, *568*, 1–98. [CrossRef]
7. Horndeski, G.W. Second-order Scalar-tensor Field Equations in a Four-dimensional Space. *Int. J. Theor. Phys.* **1974**, *10*, 363–384. [CrossRef]
8. Sushkov, S.V. Exact Cosmological Solutions with Nonminimal Derivative Coupling. *Phys. Rev. D* **2009**, *80*, 103505. [CrossRef]
9. Vainshtein, A.I. To the Problem of Non-Vanishing Gravitation Mass. *Phys. Lett. B* **1972**, *39*, 393–394. [CrossRef]
10. Abbott, B.P.; Abbott, R.; Abbott, T.D.; Acernese, F.; Ackley, K.; Adams, C.; Adams, T.; Addesso, P.; Adhikari, R.X.; Adya, V.B.; et al. GW170817: Observation of Gravitational Waves from a Binary Neutron Star Inspiral. *Phys. Rev. Lett.* **2017**, *119*, 161101. [CrossRef] [PubMed]
11. Ezquiaga, J.M.; Zumalacárregui, M. Dark Energy After GW170817: Dead Ends and the Road Ahead. *Phys. Rev. Lett.* **2017**, *119*, 251304. [CrossRef] [PubMed]
12. Creminelli, P.; Vernizzi, F. Dark Energy After GW170817 and GRB 170817A. *Phys. Rev. Lett.* **2017**, *119*, 251302. [CrossRef] [PubMed]
13. Romano, A.E.; Sakellariadou, M. Interpreting the Modified Gravitational Wave Speed in Terms of a Time Delay. *Phys. Rev. Lett.* **2023**, *130*, 231401. [CrossRef] [PubMed]
14. Romano, A.E. Constraining the effective field theory of dark energy with multimessenger astronomy. *Phys. Rev. D* **2025**, *111*, 084086. [CrossRef]
15. Brout, D.; Scolnic, D.; Popovic, B.; Riess, A.G.; Carr, A.; Zuntz, J.; Kessler, R.; Davis, T.M.; Hinton, S.; Jones, D.; et al. The Pantheon+ Analysis: Cosmological Constraints. *Astrophys. J.* **2022**, *938*, 110. [CrossRef]
16. Scolnic, D.; Brout, D.; Carr, A.; Riess, A.G.; Davis, T.M.; Dwomoh, A.; Jones, D.O.; Ali, N.; Charvu, P.; Chen, R.; et al. The Pantheon+ Analysis: The Full Dataset and Light-curve Release. *Astrophys. J.* **2022**, *938*, 113. [CrossRef]
17. DESI Collaboration. DESI 2024 VI: Cosmological Constraints from the Measurements of Baryon Acoustic Oscillations. *arXiv* **2024**, arXiv:2404.03002. [CrossRef]
18. Bertotti, B.; Iess, L.; Tortora, P. A Test of General Relativity using Radio Links with the Cassini Spacecraft. *Nature* **2003**, *425*, 374–376. [CrossRef] [PubMed]
19. Romano, A.E. The effects of dark energy on the matter-gravity coupling. *arXiv* **2025**, arXiv:2511.15049. [CrossRef]